Hybrid 6-DoF Magnetic Localization for Robotic Capsule Endoscopes Compatible With High-Grade Magnetic Field Navigation

FEDERICO BIANCHI[1,2], **ANTONINO MASARACCHIA**[1,3], **(Member, IEEE),**
ANGELO DAMONE[1,2], **ERFAN SHOJAEI BARJUEI**[1,4],
CALOGERO MARIA ODDO[1,2], **(Senior Member, IEEE), PAOLO DARIO**[1,2], **(Life Fellow, IEEE),**
AND GASTONE CIUTI[1,2], **(Senior Member, IEEE)**

[1] The BioRobotics Institute, Scuola Superiore Sant'Anna, 56127 Pisa, Italy
[2] Department of Excellence in Robotics and AI, Scuola Superiore Sant'Anna, 56127 Pisa, Italy
[3] School of Electronics, Electrical Engineering and Computer Science, Queen's University Belfast, Belfast BT3 9DT, U.K.
[4] Advanced Robotics, Istituto Italiano di Tecnologia (IIT), 16163 Genoa, Italy

Corresponding author: Gastone Ciuti (gastone.ciuti@santannapisa.it)

ABSTRACT The paper proposes a hybrid 6 degrees of freedom localization system for endoscopic magnetic capsules, compatible with external high-grade permanent magnetic locomotion. The proposed localization system, which is able to provide an accurate estimation of the endoscopic capsule pose, finds application in the robotic endoscopy field to provide efficient closed-loop navigation of a magnetically-driven tethered capsule. It takes advantage of two optimization steps based on a triangulation approach, *i.e.* (1) mathematical approximations of the magnetic field, and (2) minimization of the magnetic field mean square deviation. The proposed localization system was tested in two different *in-vitro* scenarios for mimicking the clinical cases that a magnetic capsule would encounter during tele-operated magnetic navigation. The development phase was preceded by an in-depth work-space analysis to lay the groundwork for the localization design and implementation. Results of the hybrid 6 degrees of freedom localization system show a significant accuracy in accordance with the state-of-the-art, *i.e.* about 5 mm in position and 5° in orientation, but introducing benefits in expanding the work-space by increasing the number of electromagnets onto the operating table, as an independent solution with respect to the external magnetic locomotion source.

INDEX TERMS Capsule endoscopy, magnetic-based navigation and localization, magnetic field models, minimally-invasive colonoscopy, robotic endoscopy.

I. INTRODUCTION

A. MEDICAL EVIDENCE AND CLINICAL NEEDS

According to the most recent statistical data analysis of cancers provided by the Global Cancer Observatory in 2020, gastrointestinal (GI) cancer (including colorectum, stomach, and esophagus) can be identified as the first cause of death for cancer worldwide [1]. Indeed, every year more than 3 million new GI cancer cases and more than 2 million GI cancer deaths are counted, representing 19.5% of the global deaths by cancer. Furthermore, in the next two decades, the number

The associate editor coordinating the review of this manuscript and approving it for publication was Wei Xu.

of new GI cancer cases and deaths is expected to increase by almost 70% and 76%, respectively [2]. The most common GI cancer is colorectal cancer (CRC) which, among all other types of GI cancers and for all genders, represents the second and third most common cause of cancer death and cancer incidence worldwide, respectively [1].

Early-stage diagnosis represents one of the most promising solutions to reduce CRC mortality. Indeed, based on a study conducted by the American Cancer Society on people with diagnosed colon and rectum cancers, the 5-year survival rates combined among all surveillance, epidemiology, and End Results (SEER) stages are 64% and 67% for colon and rectal cancers, respectively. However, for both types of cancer,

it was observed how the 5-year survival rates decrease with the progression of the pathology, dropping from 90% for a localized SEER stage to 15% in case of a distant SEER stage [2]. As a result, mass screening programs play a key role in CRC early detection, especially for high-risk groups of people, such as over 50 years old persons or people with a CRC family history [3]. These programs consist of the direct visualization of the GI tract through the adoption of conventional endoscopic techniques, which represent the gold standard in the context of CRC screening and treatment. However, the efficiency of mass screening programs in CRC early detection is currently limited by the low level of patients' adherence. Usually, these deficiencies are caused by the fear of pain or the discomfort that could be perceived during an endoscopic procedure, mainly due to complex GI tracts and unskilled practitioners. Furthermore, it is worth noting that conventional endoscopes cannot examine the entire GI tract by not being able to reach the central GI sector, *i.e.* the lower small bowel [4]. A brief review of the current state-of-the-art on wireless capsule endoscopes and localization strategies is proposed in sub-sections I-B and I-C, respectively.

B. WIRELESS CAPSULE ENDOSCOPES AND SMART ROBOTS FOR PAINLESS COLONOSCOPY

During the last two decades, the possibility to develop smart robotic solutions aimed to enhance performance and increase patients' acceptability, particularly for GI inspection and treatment of endo-intestinal pathologies, *i.e.* polyps, diverticulitis, and cancer, has gained considerable attention from both industrial and academic sectors.

In 2001, the Food and Drug Administration (FDA) approved the use of a pill-size wireless device, named PillCam® [5], *i.e.* an innovative wireless technology for the inspection of the small bowel, developed by Given Imaging Ltd. (Yokneam Illit, Israel, now Medtronic Inc., Minneapolis, Minnesota, USA). This innovative technology consists of an ingestible non-actuated capsule that can visually screen the small bowel. In order to perform the screening, it was, and is still today, equipped with: (1) an LED-based illumination system, (2) a CMOS vision sensor, (3) coin batteries, and (4) a radio frequency (RF) module used to transmit data and track the capsule inside the human body through external antennas. This type of wireless capsule endoscopy (WCE) was able to achieve a massive disruption in clinical practice and in the market by solving a problem never faced before, *i.e.* the examination of the lower small bowel. In addition, this revolutionary technology represented an efficient solution to address the fear of pain, discomfort, and feelings associated with conventional endoscopic procedures. The same principle was adopted to develop WCE-based solutions for the upper-GI tract and colonic screening [6], [7]. However, in the latter case, WCEs resulted less effective and reliable in terms of overall lesion detection rate [8]–[10]; the main cause can be identified in the different anatomical features of each GI tract. In fact, the small intestine can be considered

a long tubular lumen with an average diameter similar to the endoscopic capsules; then, the alignment between the capsule and the small intestine tract can be guaranteed. On the contrary, the colorectal tract is larger and more collapsed than the small intestine. Therefore, it cannot be entirely and adequately screened by a passive-locomotion pill-sized device. However, the key role of this innovative methodology is to reduce the discomfort and pain associated with conventional endoscopy, even if a preparation procedure is still required. Indeed, taking inspiration from this method, many wireless and wired capsule endoscopes were developed; details about innovative wireless and wired capsule endoscopes are reported in [6], [7], [11]–[13]. The most promising solution for painless colonoscopy, as agreed upon by the scientific community and from the authors' consideration, is the magnetically-driven approach developed starting from 2009 by Ciuti *et al.* [14]. Over the years, many researchers have made many improvements in terms of embedded functionalities, navigation, and localization [15]–[19]. Generally, a magnetically-driven capsule colonoscope is composed of: (1) a capsule, (2) a soft tether, (3) a robotic-driving tele-operated platform, and (4) acquisition and process units. The capsule embeds: (1) a LED-based illumination and high-definition vision module, (2) an internal permanent magnet (IPM), and (3) a set of MEMS sensors used for localization. The soft tether represents the connection between the capsule's body and the external control unit, passing power supply for the internal electronics, data transmission, and embedding service channels for conventional endoscopic functionalities. Externally, a robotic arm, driving a permanent external magnet (EPM) attached to the end-effector, and a localization system forms the master-slave tele-operated robotic platform. The soft-tethered capsule is moved and oriented within the colonic lumen through the interaction between the two permanent magnets (*i.e.*, IPM-EPM). This promising technology benefits from both WCE and conventional endoscopes. Indeed, although WCE is painless, it cannot perform either treatment and accurate diagnosis in the colonic tract due to the lack of an active capsule control, proper distension of the lumen, high-definition camera, and other interventional functionalities. On the other hand, a magnetic-actuated capsule, such as for the conventional endoscope, can be controlled in a distended colon and can perform cleaning and treatment through the operating channel. In addition, the soft tether of the magnetic-actuated capsule can be deformed enough to not stretch the anatomical structure of the colon due to the change of the actuation paradigm, *i.e.* from a "rear-wheel" to a "front-wheel" driving approach. In fact, the body shaft must be rigid enough to avoid curling the conventional endoscope on itself as it is pushed and pulled from the outside of the patient. However, magnetic actuation has increased the system's complexity. To accurately and reliably navigate the capsule, knowledge of the relative pose between the EPM and the capsule's IPM is required. Unlike manual colonoscopy, where the colonoscope is forced to follow the

colon's lumen under external force/pressure, the knowledge of the capsule pose is necessary to guarantee a no-contact closed-loop robotic navigation and allow to gather knowledge for follow-up interventions.

C. LOCALIZATION STRATEGIES FOR CLOSED-LOOP CONTROL: BACKGROUND AND KEY EXAMPLES

Localization strategies for magnetic endoscopic capsules can be categorized into two main classes: (1) localization strategies not compatible, and (2) compatible with external high-grade magnetic field actuation sources for the endoluminal capsule robot's navigation.

The first localization strategy class is almost exclusively applied to conventional WCE. Since 2005, *The Chinese University of Hong Kong* [20] has developed a localization strategy with a sophisticated sensing module outside the capsule that embeds a small permanent magnet used as a transmitter. This localization strategy has been improved in the following years, using a permanent magnet embedded inside the capsule that generates a static magnetic field detected by a set of wearable Hall-effect sensors located outside the patient's body [21]. Increasing the number of sensors, the accuracy of the localization increases. The average deviation of this 6 degrees of freedom (DoF) localization strategy is under 5 mm and 3° in position and orientation, respectively. An improved configuration, published by the same authors in 2020 [22], detects the displacement of the embedded small permanent magnet when it exceeds a pre-defined threshold. Subsequently, a localization sensor array is automatically moved using a servo platform according to the detected displacements below the magnetic source. This solution allows keeping the sensors consistently below the small permanent magnets to avoid losing accuracy. The accuracy in position and orientation obtained with this approach has been improved to 2.04 mm and 2.45°, respectively. A different magnetic-based solution, belonging to the same class, is composed of one or more coils embedded into the capsule, and several alternating-current electromagnets (EMs; also used for Electromagnetic) placed outside the patient body [23]–[25]. This localization strategy is frequently used because it allows reaching position and orientation errors under 1 mm and 1°, respectively. Commercially-available technologies, *e.g.* the Northern Digital Inc. (Ontario, Canada) electromagnetic tracking systems, exploit a similar approach, in which external electromagnetic coils act as the transmitter for miniaturized wired 5-DoF or 6-DoF sensors [26]. However, all the aforementioned localization strategies cannot be used with external high-field magnetic sources because the embedded sensors are limited in the measurement range, or the noise/interference is excessive if compared to the signal. The second class among localization strategies is usually implemented for active magnetic-locomotion capsules. The most notable solution was developed starting from 2005 by the *Scuola Superiore Sant'Anna* (Pisa, Italy) [14], [18] and, following a similar approach, improved by the *University*

of Leeds (Leeds, UK). The latest layout of the system is represented by a hybrid solution composed of a robotic arm that holds on its end-effector an EM and an EPM used to drive and localize a soft-tethered active-locomotion capsule [17]. A similar solution was developed, in 2013, by the *University of Utah* (Salt Lake City, UT, USA), and it consists of an alternating magnetic field-based closed-loop navigation. The solution employs a permanent rotational magnet held on the end-effector of a 6-DoF robotic arm that allows both the navigation and localization of the capsule [27]. Differently from the solution proposed by the *University of Leeds*, the spiral-shape capsule is propelled by applying an angular rotation to a rotating permanent magnet. The capsule is equipped, in either cases, with six Hall-effect sensors, and with an inertial sensor. Both 6-DoF solutions can localize the capsule with an average deviation lower than 5 mm and 6° in position and orientation, respectively. In addition, the previous solutions have a hemispherical operating range centered on the EPM and limited to the locomotion workspace of the capsule. This limitation exists because a single magnetic source attached to the robotic end-effector (*i.e.*, the EPM and/or the EM) is used to move and localize the endoscopic capsule. Finally, a similar and more recent solution, developed by the *The Chinese University of Hong Kong* [28], demonstrated how to localize a capsule embedding two ring-shaped magnets actuated by a high-grade external magnetic field rotating EPM. In this case, the magnetic fields generated by the three magnets (*i.e.*, two ring magnets and one EPM) are measured by external Hall-effect sensors and, using an unscented Kalman filter, the magnetic field contributions are extracted to localize the capsule's pose. This solution allows the estimation of the capsule's pose with an average deviation lower than 6 mm and 6° in position and orientation, respectively.

D. AIM OF THE STUDY AND ORGANIZATION OF WORK

The authors propose a hybrid magnetic localization system, developed in the context of the H2020 European *"Endoscopic versatile robotic guidance, diagnosis, and therapy of magnetic-driven soft-tethered endoluminal robots"* (Endoo) Project [29], [30]. In particular, the hybrid 6-DoF magnetic localization system, based on an EM-enabled solution, has been designed to be compatible with external high-grade magnetic field sources used for actuation and navigation of magnetically-driven devices, but without depending on them. In particular, the proposed solution: (1) allows having a flexible and expandable work-space based on the position and number of the EM field sources integrated, as a stand-alone module, into the operative table and under the patient, and (2) guarantees to locate the capsule even if it is distant from the high-grade magnetic field source, *i.e.* the EPM used for actuation and navigation. This solution avoids initial scanning procedures through the movement of the robotic arm on the patient to find the capsule. In addition, the proposed localization system includes a dual-step optimization method to enhance both the localization accuracy and the computational

time necessary for the real-time estimation of the capsule's pose. In particular, the first optimization step takes advantage of ellipsoidal and spherical mathematical approximations to precisely model the magnetic field generated by the external sources in the 3D space. On the other hand, the second optimization step exploits an accurate analytical magnetic model to iteratively minimize the root mean square deviation (RMSD) between the measured and estimated magnetic fields. In summary, the first step provides a rough estimation of the capsule position but is less affected by local minima, while the second step provides a more accurate estimation but is slower and more affected by the local minima. Moreover, the proposed optimization solution emphasizes the importance of applying a weight to magnetic field measurements to increase the pose estimation accuracy. Finally, we propose a method for estimating the measurement errors and explaining how to take them into the capsule's pose estimation phases.

The rest of the paper is organized into three remaining sections. Section II presents the localization strategy and the experimental setup for validation. Then, obtained results are presented in Section III and, finally, the discussion and the conclusions are reported in Section IV. It is worth mentioning that the system developed in this work has been patented [31].

II. MATERIALS AND METHODS

In this section, the procedure adopted for the design of the proposed 6-DoF localization system is illustrated. The section is divided into three sub-sections. Sub-section II-A briefly introduces the general architecture of the magnetically-driven robotic platform for colonoscopy in order to give a comprehensive view of the tele-operated robotic platform, while the proposed localization strategy and implemented algorithm are provided in sub-section II-B and sub-section II-C, respectively. Finally, sub-section II-D describes the experimental set-ups and methodologies adopted to validate the performances of the proposed 6-DoF magnetic localization strategy.

A. GENERAL ARCHITECTURE OF THE ROBOTIC PLATFORM AND CONSTITUTIVE MODULES

The primary purpose of the proposed magnetically-driven robotic platform is to introduce painless colonoscopic technology by improving the overall target population's acceptance. In order to achieve this ambitious goal, the overall design and development procedure consisted of: (1) an estimation of the operative work-space for magnetic locomotion and localization, (2) the design and development of a localization module able to compute, in real-time, the position and orientation (6-DoF) of an endoscopic capsule compatible with the high-grade field magnetically-driven colonoscopy, and (3) the design and development of a locomotion module to magnetically navigate a soft-tethered capsule in the colorectal tract. The first two aspects will be described in this paper, focusing on the localization module. Furthermore, the paper will briefly provide an overall comprehension

of the magnetic design for locomotion purposes and the magnetically-driven robotic platform. Still, implementations and details are already available and described in [29], [32].

In order to obtain the volume of a typical operative work-space, 3D reconstructions of human colorectal tracts were performed with computer vision tools. In particular, such volumetric reconstructions were obtained using an open-source dataset of 30 computerized colon tomographies (CCT), extracted from a public repository [33]. As illustrated in Figure 1, each CCT slice of the dataset was used to evaluate both the distances between the upper wall of the colon and the back and front sides of the human's skin, by considering only the upper point if the colon intersected a single slice more than one time. It is worth noting that the upper wall of the colon was used in the data analysis because it is assumed that, with our single-magnet robotic approach, the endoscopic capsule is magnetically-attracted by an EPM moved above the upper abdominal side (Figure 2). Then, the operating distances for locomotion and localization were obtained as an average of these measurements in the dataset.
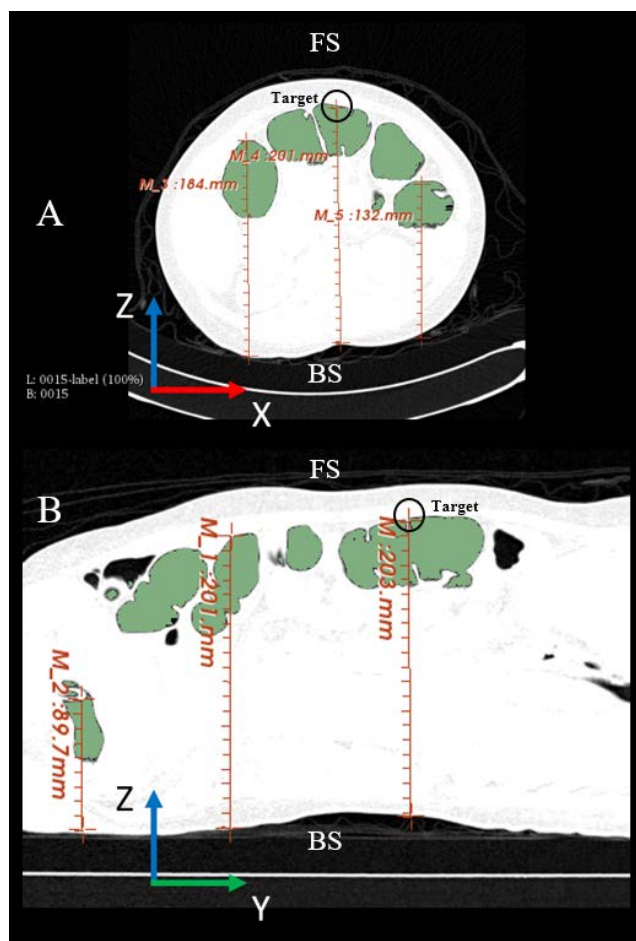

FIGURE 1. Example of the identification of the upper surface of the segmented colon - (A) axial and (B) sagittal views - in a typical CCT slice and distance calculation to the back side (BS, for the localization work-space) of the human's skin; FS: front side, for the locomotion work-space.
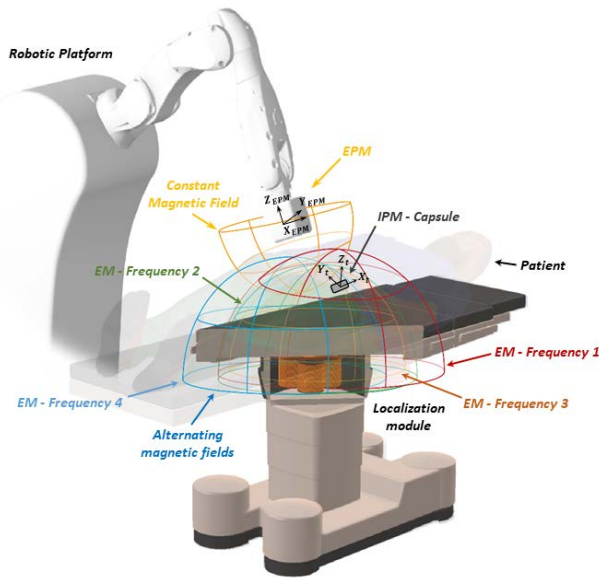
FIGURE 2. General overview of the tele-operated robotic endoscopic platform with details of the endoscopic capsule with the internal permanent magnet (IPM), and of the magnetic field distributions generated by both the external permanent magnet (EPM) and four electromagnetic (EM) sources operating at different frequencies.

Each volumetric colon was manually reconstructed using 3D Slicer software (Harvard University, Cambridge, USA), whereas the distances and the work-space measurements were evaluated using a Matlab code (MathWorks, Massachusetts, USA).

As illustrated in Figure 2, an EM-based solution composed of four coils, installed below the operating table, was selected for the design of the proposed localization module. As explained in the following sections, this choice was motivated by the need to: (1) simultaneously operate at different frequencies, thanks to the different EM sources, for real-time triangulation, (2) generate variable magnetic field magnitudes compatible with the operating works-space and sensor measurement range, (3) avoid interference with the EPM static magnetic field used for locomotion, and (4) be flexible in expanding the work-space by simply integrating additional coils.

The locomotion module consists of a 6-DoF anthropomorphic robotic arm equipped with an EPM placed at its end-effector. The endoscopic capsule is moved by exploiting the EPM-IPM magnetic interaction forces and torques. The EPM is a diametrically-magnetized, circular-shape, N52-grade NdFeB magnet (magnetization of 1.45 A/m), with a diameter of 90 mm and a length of 80 mm, resulting in a total volume of about 508 cm^3. On the other side, the IPM is a semi-circular axially-magnetized N52 grade NdFeB magnet (magnetization of 1.45 A/m) with a diameter of 17 mm and a length of 25 mm length, resulting in a total volume of about 2.83 cm^3. These values were adequately chosen in order to maximize the EPM-IPM magnetic force interaction for ensuring the correct navigation of the capsule in the colorectal tract at operating distances of about 100 mm, but also taking into consideration the allowed payload and

dimensions of the magnetic sources for the selected robotic arm [32]. An illustration of the robotic platform, including the localization and locomotion modules, is provided in Figure 2.

B. LOCALIZATION MODULE

As mentioned before, the localization of the capsule was obtained using a set of four EM sources integrated into the lower side of the operating table, under the patient (see Figure 2), generating alternating magnetic fields at four different frequencies. Sensing the intensity of these alternating fields and the intensity of the static magnetic field generated by the EPM, the 6-DoF pose of the endoscopic capsule can be estimated by exploiting a triangulation approach. As a result, the localization module can be further divided into three main sub-modules: (1) an electromagnetic field generator module (sub-section II-B1), (2) a sensing module (sub-section II-B2), and (3) a signal processing module (sub-section II-B3). Figure 3 shows the organization of the modules, with their components, within the robotic platform and the representation of axes and angles, which define the capsule location and orientation.

1) ELECTROMAGNETIC FIELD GENERATOR MODULE

This sub-module generates alternating magnetic fields at different frequencies by providing the proper alternating current to a set of four coils, which act as EMs. According to the Biot-Savart's law (equation 1), the magnetic field generated by an element of a conductor carrying current results:

$$\mathbf{B}(\mathbf{r}) = \frac{\mu_0 I_c}{4\pi} \int_C \frac{\mathbf{dl} \times (\mathbf{r} - \mathbf{r}')}{|\mathbf{r} - \mathbf{r}'|^3} \tag{1}$$

where μ_0 represents the air magnetic permeability, $\mathbf{dl}$ is the infinitesimal vectorial length of the element carrying a current I_c, $\mathbf{r}$ is the reference point at which the magnetic field $\mathbf{B}(\mathbf{r})$ is measured, and $\mathbf{r}'$ is the vectorial position of the infinitesimal current element that contributes to the total magnetic field. A more detailed analytical model for the magnetic field distribution of both the permanent magnet and electromagnet is reported in the Appendix section [34]. In particular, combining the results obtained and reported in sub-section II-A, about the assessment of the operating distances with the magnetic modeling of the electromagnets introduced in the equation 1, it was possible to derive the dimensions of the operating work-space and to find the optimal size of the EMs. Therefore, the derived specifications of the EMs are summarized with the following parameters, *i.e.* height (H: 100 mm), internal and external radii (R_i: 22 mm and R_e: 50 mm), diameter of the wire (ϕ: 1.8 mm), maximum operative current (I_c: 16 A), and working frequencies (f: 70, 80, 90, 100 Hz for each EM, respectively).

In order to drive the proper current into each coil, as illustrated in Figure 3, we used a set of power inverters to transform the direct current (DC) provided by the power supply into the corresponding alternating current (AC). Each inverter
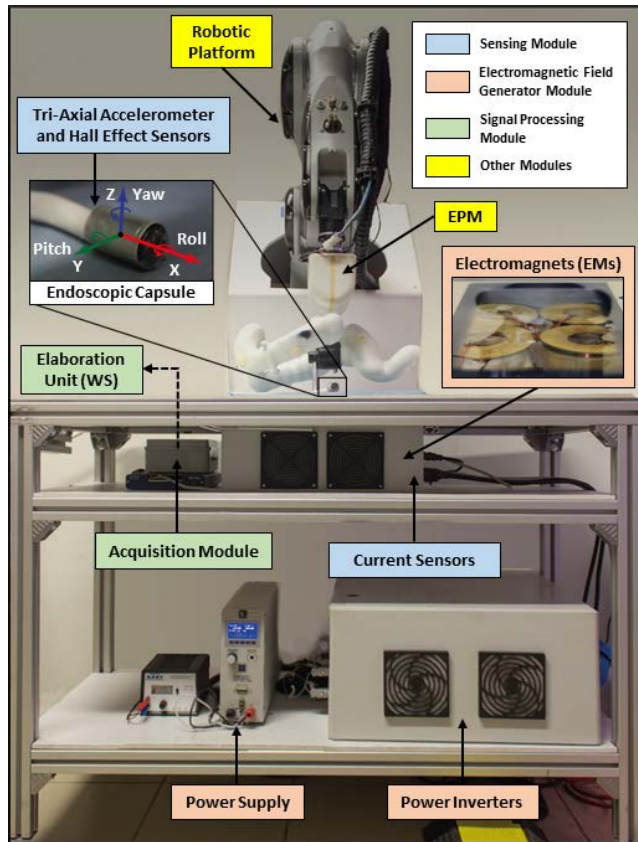
FIGURE 3. Overview of the platform, showing the constitutive localization modules and the direction axes for the roll, pitch and yaw angles.

was driven by an appropriate signal, generated using an industrial controller (IC-3173) produced by the National Instrument company (NI - Austin, Texas, U.S.A.), and programmed by a dedicated LabVIEW code compiled into its FPGA unit. Modeling each coil as a purely inductive load, the relationship between the applied AC voltage and the corresponding AC current in a sinusoidal regime is expressed with the following relation (equation 2):

$$I_c = \frac{V_c}{2\pi f L} \tag{2}$$

where f represents the frequency, L the coil's inductance, and V_c the voltage set. Then, since each power inverter applies the same output voltage at different frequencies, each coil has a different current flow sensor that generates a magnetic field with different intensity (see sub-section II-B2). For this reason, each coil is equipped with a dedicated current sensor to measure, periodically, and then control, in a closed-loop, the current flowing in it.

2) SENSING MODULE

The sensing module (Figure 3) is responsible for measuring and providing data, *i.e.* (1) intensity of the magnetic fields within the operational work-space, (2) induced accelerations on the endoscopic capsule, and (3) currents flowing on each coil, which are subsequently elaborated to estimate the 6-DoF position and orientation of the capsule. In order to achieve this

purpose, the sensing module consists of two parts: (1) the first one, embedded in the endoscopic capsule, and (2) the second one, connected to the EMs.

The capsule-embedded part comprises a tri-axial Hall-effect sensor to measure the intensity of the external magnetic fields and a tri-axial accelerometer sensor to measure the acceleration induced to the capsule due to the EPM-IPM magnetic interaction. In order to obtain a good trade-off between measurement range and resolution, a Low Power 3D Hall-effect Sensor TLE493D-W2B6 (Infineon Technologies, Neubiberg, Germany) was embedded, which has a measurement range of ±200 mT and a 12-bit data resolution in each measurement direction. It is worth mentioning that the relative position between the IPM and the Hall-effect sensor inside the capsule was selected to minimize the offset contribution of the internal magnetic field source, (*i.e.*, the IPM, avoiding the saturation of the sensor along with all measurement directions). Regarding the accelerometer, the ultra-low-power high-performance IIS2DH sensor from STMicroelectronics (STMicroelectronics, Geneva, Switzerland) was integrated, with a measurement range of ±16 g and a 12-bit data resolution for each measurement direction.

As regards the second part, it consists of four split core current transformer SCT-013 (Dechang Electronic Co., Ltd Beijing, China) used to measure the current flowing in each coil and then estimating the intensity of the magnetic field generated by each electromagnet, according to the principle of mutual induction on a secondary coil.

3) SIGNAL PROCESSING MODULE

The signal processing module (Figure 3) consists of an acquisition module dedicated to collecting data coming from the sensing module and forwarding them to an elaboration unit through a USB connection with a sampling period of 300 ms. In particular, the acquisition module comprises a set of acquisition boards, where each of them works independently from the others. The data acquisition boards are organized as follow:

1) an Infineon TLE4922 MS2GO board, interfaced with the 3D Hall-effect sensor, programmed to send data at a sampling frequency of 330 Hz with a 12-bit data resolution;
2) an Arduino Due board (Arduino, Somerville, Massachusetts, U.S.A.), which acquires data from the tri-axial accelerometer and programmed to send it at a sampling frequency of 400 Hz with a 12-bit data resolution;
3) a NI board USB X Series Multi-functional DAQ, which manages the analog measurement from the current sensors, sending them at a sampling frequency of 1 kHz with a 12-bit data resolution.

The elaboration unit is made by a workstation machine (WS) that receives the data from these acquisition boards and runs the localization algorithm to estimate the 6-DoF capsule position and orientation.
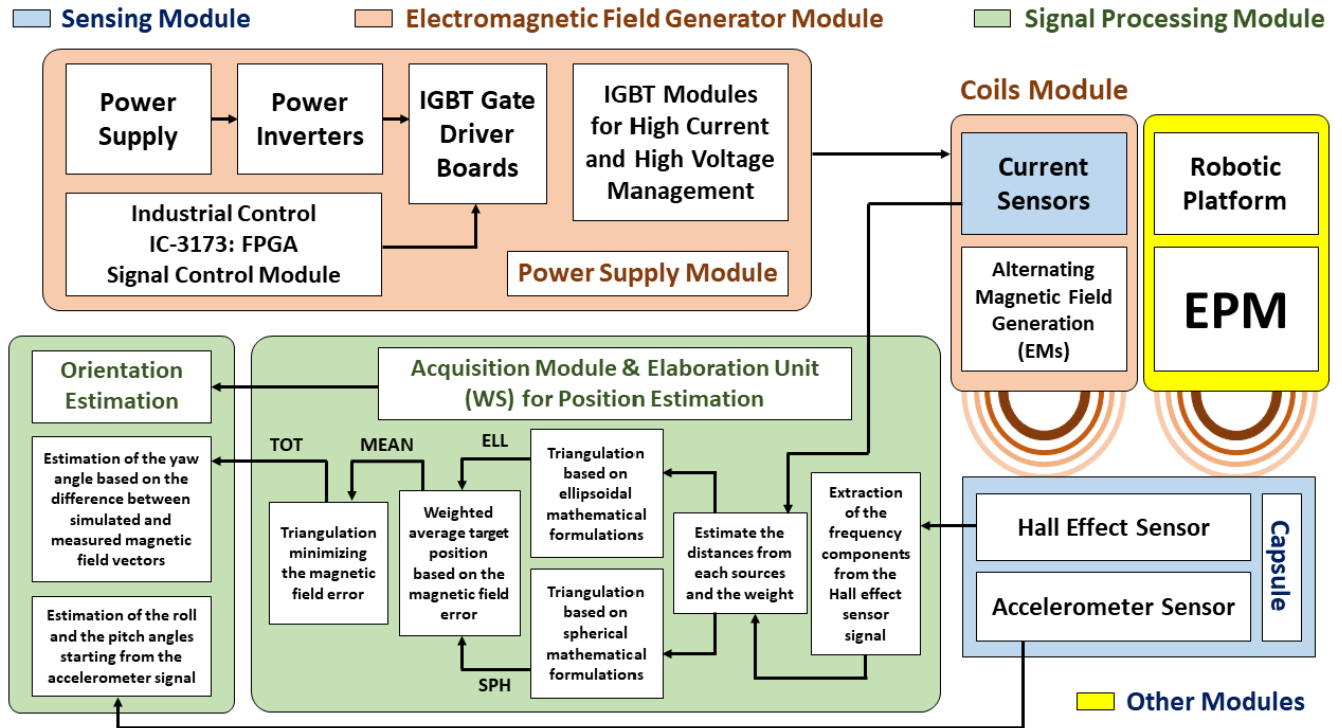
FIGURE 4. Operating diagram and workflow of the localization system; IGBT stands for Insulated Gate Bipolar Transistor and FPGA stands for Field Programmable Gate Array.

C. LOCALIZATION ALGORITHM

As mentioned in Section II-B3, the elaboration unit executes the localization algorithm, which processes the measured multi-modality data providing the 6-DoF pose of the capsule. In particular, the proposed algorithm consists of two elaboration steps in order to derive the pose of the endoscopic capsule, *i.e.* (1) a 3-DoF position estimation, and (2) a 3-DoF orientation estimation. The entire procedure is summarized in the green box illustrated in Figure 4, and every single step will be described below.

1) 3-DoF POSITION ESTIMATION

Once the x, y, and z components of the magnetic field signals are acquired by the tri-axial Hall-effect sensor, the oscillating components generated by each coil are extracted through a Discrete Fourier Transform (DFT) [35] with 1000 samples window, while the static components of the EPM are estimated as the average over the sample window for all the three directions. Based on the intensity of each oscillating and stationary component, combined with current measurements, an early-rough estimation of the distances between each magnetic source and the endoscopic capsule was calculated from the scalar value of the magnetic field intensity, coming from every single source. This first estimation stage was performed using logistic functions where the parameters have been obtained by comparing the analytical magnetic model [34] and measured values of the magnetic field. The development of these logistic functions is essential to correlate the distance and the scalar

intensity of the magnetic field for each kind of source for all the x, y, and z components (see Appendix section for further details). These logistic approximations are necessary to preliminary assess the distances based on the magnetic field's scalar intensity and efficiently perform all the calculations.

Subsequently, the triangulation approach aims to estimate the position of the endoscopic capsule using a spherical and an ellipsoidal approximation starting from the position calculated in the previous step through the logistic functions. At this scope, it was noticed that adopting the spherical approximation, an over-estimation of the distance between the sources and the capsule was observed. At the same time, an under-estimation was obtained using an ellipsoidal approximation. Therefore, to address this issue, it has been proposed to solve the triangulation problem for each approximation model, obtaining a two-position evaluation, *i.e.* spherical ($\mathbf{r}_{SPH}$) and ellipsoidal ($\mathbf{r}_{ELL}$) approximate vectorial positions of the endoscopic capsule. For this purpose, the following objective functions (equations 3-4) have been developed to find the two vectorial positions starting from the estimated distances in the previous step:

$$min_i(SPH) = \sum_{n=1}^{N_S} w_n \left[\left(\frac{x_t^i - x_n^{SR}}{d} \right)^2 \right.$$
$$\left. + \left(\frac{y_t^i - y_n^{SR}}{d} \right)^2 + \left(\frac{z_t^i - z_n^{SR}}{d} \right)^2 \right] \quad (3)$$

$$min_i(ELL) = \sum_{n=1}^{N_S} w_n \left[\left(\frac{x_t^i - x_n^{SR}}{d_\perp} \right)^2 + \left(\frac{y_t^i - y_n^{SR}}{d_\perp} \right)^2 + \left(\frac{z_t^i - z_n^{SR}}{d_\parallel} \right)^2 \right] \quad (4)$$

where the subscript n represents the nth magnetic source, while the subscript t refers to the endoscopic capsule. In addition, SR represents the system reference of each source, the index i represents the optimization step on the endoscopic capsule position components for spherical and ellipsoidal approximations, and N_S indicates the total number of magnetic sources. In the case of the ellipsoidal approximation, there are two estimated components, *i.e.* a normal ($d_\perp$) and a parallel distance ($d_\parallel$) to the main axis of the coils, while in the case of the spherical approximation the parameter d is equal to $max(d_\perp, d_\parallel)$. It is important to highlight that $d_\perp$ and $d_\parallel$ are computed in the first step through the magnetic field measurement. The term w_n represents the weight assigned to each source according to the slope of the magnetic field intensity using the corresponding logistic function that approximates the analytical model (details are provided in Appendix section). This ensures that each magnetic source is weighted according to the distance between the magnetic source and the endoscopic capsule during the optimization phase. In particular, the weight reduces the error in estimating the capsule position by ∼20% as it prevents distant and, therefore, less accurate sources from overly influencing the position estimation. The optimization algorithm developed and used in this work is a non-linear solver [36] that minimizes the objective function introduced in the equations 3-4.

Once the objective functions 3-4 have been minimized, the two estimated spherical ($\mathbf{r}_{SPH}$) and ellipsoidal ($\mathbf{r}_{ELL}$) vectorial positions were used to calculate the intensities of the magnetic field using the analytical models for both EMs and EPM. The deviation between the calculated intensities of the magnetic field and the measured data by the Hall-effect sensors has been used to calculate a new corrected averaged position ($\mathbf{r}_{MEAN}$) of the capsule based on the spherical and ellipsoidal approximation (equation 7):

$$\Delta B_{SPH} = \frac{1}{N_S} \sum_{n=1}^{N_S} \left(|\mathbf{B_n}(\mathbf{r}_{SPH})| - |\mathbf{B_n^m}| \right) \quad (5)$$

$$\Delta B_{ELL} = \frac{1}{N_S} \sum_{n=1}^{N_S} \left(|\mathbf{B_n}(\mathbf{r}_{ELL})| - |\mathbf{B_n^m}| \right) \quad (6)$$

$$\mathbf{r}_{MEAN} = \frac{\Delta B_{SPH}^{-1} \mathbf{r}_{SPH}}{\Delta B_{SPH}^{-1} + \Delta B_{ELL}^{-1}} + \frac{\Delta B_{ELL}^{-1} \mathbf{r}_{ELL}}{\Delta B_{SPH}^{-1} + \Delta B_{ELL}^{-1}} \quad (7)$$

where $\mathbf{B_n}(\mathbf{r}_{SPH})$ represents the vectorial magnetic field intensity for the nth source calculated at $\mathbf{r}_{SPH}$ in the spherical approximation, $\mathbf{B_n}(\mathbf{r}_{ELL})$ represents the vectorial magnetic field intensity for each source calculated at $\mathbf{r}_{ELL}$ in the ellipsoidal approximation, and $\mathbf{B_n^m}$ indicates the measured magnetic field for each source. The terms ΔB_{SPH} and ΔB_{ELL}

represent the average absolute deviations between the calculated magnetic field in the previous optimization stage and the measured data for both SPH and ELL approximations.

The final step of the position estimation stage is represented by an optimization that starts from the estimated averaged position $\mathbf{r}_{MEAN}$ of the endoscopic capsule, and minimizes the RMSD between the measured magnetic field and the magnetic field generated by each source according to their analytical magnetic model [34], presented in sub-section II-B and in the Appendix section. The objective function is represented by the following equation 8:

$$min_i(RMSD) = \sum_{n=1}^{N_S} w_n \left(|\mathbf{B_n^{ei}}| - |\mathbf{B_n^m}| \right)^2 \quad (8)$$

where n represents the magnetic source, N_S indicates the total number of magnetic sources, w_n represents the weight assigned to each source based on the slope of the magnetic field intensity according to their respective parametric logistic function mentioned in the previous paragraph, and $\mathbf{B_n^{ei}}$ and $\mathbf{B_n^m}$ represent the estimated at each iteration and the measured magnetic field, respectively. The minimization of the objective function 8, allows defining the final position of the endoscopic capsule ($\mathbf{r}_{TOT}$).

2) 3-DoF ORIENTATION ESTIMATION

The orientation estimation combines the signals of the 3D accelerometer sensor, from which the pitch and roll angles are calculated, and the difference between simulated and measured magnetic field vectors of the EPM to estimate the yaw angle. In particular, it can be calculated using the following equation 9:

$$\gamma = sign \left(\frac{B_x^e}{B_y^e} - \frac{B_x^m}{B_y^m} \right) \tan^{-1} \left(\frac{\left\| \mathbf{B_{xy}^m} \times \mathbf{B_{xy}^e} \right\|}{\mathbf{B_{xy}^m} \cdot \mathbf{B_{xy}^e}} \right) \quad (9)$$

where $\mathbf{B_{xy}^m}$ and $\mathbf{B_{xy}^e}$ represent the projection on the X-Y plane of the measured and the estimated magnetic field, B_x^e and B_y^e represent, respectively, the x and y component of the estimated magnetic field, and B_x^m and B_y^m indicate, respectively, the x and y components of the measured magnetic field. It is important to state that not-observable regions do not affect roll and pitch angles because they do not depend on the magnetic field measurements. Instead, it is possible to incur not-observable singularity regions where the yaw angle cannot be adequately measured. In particular, it may happen when the measured magnetic field vector does not lie on the X-Y plane, especially when the capsule and the EPM are too distant. Consequently, the measured magnetic field signal is so weak that the instrumental noise can overlap in the not-observable regions. The non-observable region is a situation that can rarely happen, and it can be solved by re-positioning the EPM to have a new engagement that guarantees the measure of the yaw angle without losing the magnetic control of the endoscopic capsule in this region by the robotic platform.
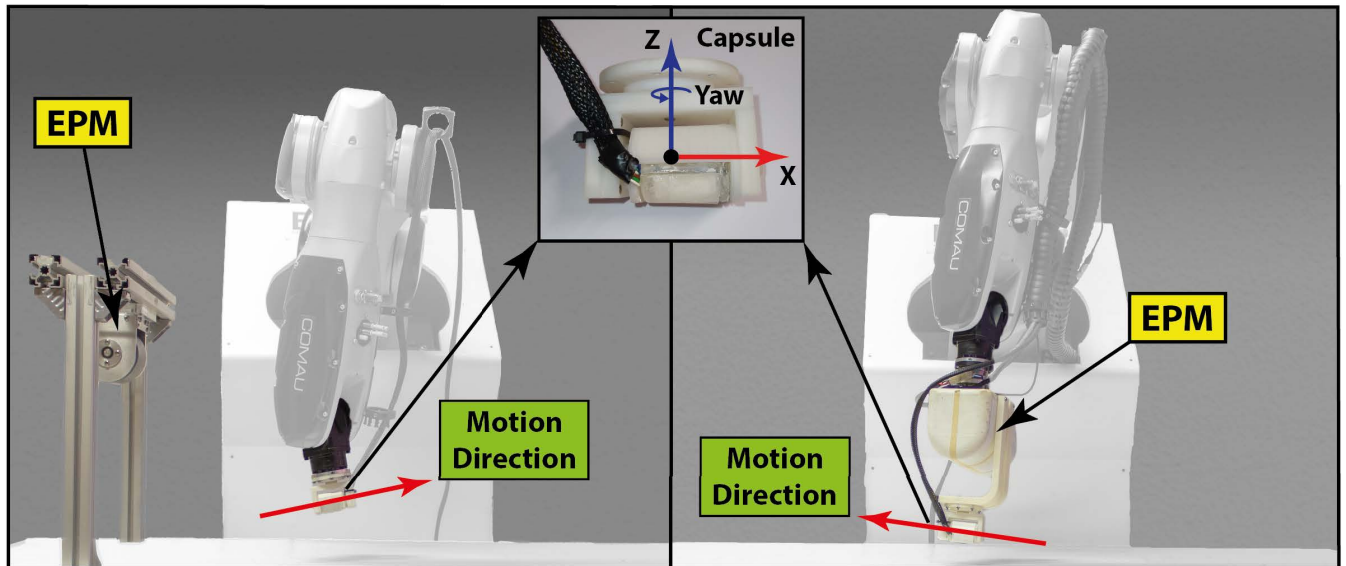
FIGURE 5. Experimental scenarios in the searching (left) and navigation test phases (right).

D. EXPERIMENTAL SESSIONS

The experimental session aims to estimate and evaluate the 6-DoF localization error in position and orientation. In a standard magnetically-driven capsule procedure, it is possible to identify two operational phases based on the reciprocal position between capsule and EPM: (1) an initial searching phase, and (2) a navigation phase. The searching phase is characterized by the condition that the relative position between the capsule and the EPM is highly variable, and it may be executed in two cases: (1) initially, when the capsule is inserted into the patient, and (2) in the situation in which the navigation must be interrupted and then resumed for any clinical needs. On the other hand, the navigation phase represents the most common stage of the entire procedure: the capsule, if fully controlled by the EPM, implies that the relative distance and orientation between them are negligible. In addition, it has been noted that the two phases are characterized by different needs based on their aims: in the searching phase, it is fundamental to know the 3-DoF capsule position in order to drive the EPM to link the capsule, but the orientation is less critical for the auto-alignment of the capsule due to the magnetic attraction, while in the navigation phase both 6-DoF position and orientation information are crucial to correctly move the capsule along the colon path with an optimal magnetic interaction.

As a result of these considerations, two sets of experiments were performed. The first set of experiments consists of the searching phase (phase 1), where the relative position of the EPM with respect to the capsule is outside the operating range. In this case, the EPM is attached to an external fixed support, while the capsule is placed on the end-effector of the robotic arm to simulate and control its pose (see Figure 5). The second set of experiments concerns the navigation phase (phase 2), where the EPM is fixed on the

robot, and it is moved consistently with the capsule, following pre-determined trajectories. Consistent motion trajectories have been extracted using a Matlab software package called Skeleton3D [37]–[39] by simply calculating the central points of the segments that identify the colon in each sectional CCT image stemming from a database of 30 patients CCT scans [33]. Subsequently, the three longest paths have been selected from the calculated trajectories in the center of the colon and chosen to conduct the experiments. The localization system is tested and analyzed during the searching and navigation stages on these realistic operating work-spaces. Specifically, details of the two phases are summarized as follow:

a) *searching phase*: the EPM is fixed externally to the operating space of the tracking system. The capsule is fixed on the robot's end-effector through a rigid support, and it is moved along three trajectories. Each trajectory is traveled 5 times for three different speeds, *i.e.* [1, 3, 5] mm/s. Since the relative distance between the EPM and the capsule will be relevant in this set of tests, the estimate of the yaw angle will not be relevant because the capsule will be in the non-observable region.

b) *navigation phase*: the EPM is fixed on the robot's end-effector with the capsule locked underneath at a distance of 100 mm, *i.e.* typical EPM-capsule operating distance. The EPM and the capsule are moved along three trajectories extracted from CCT scans. Each trajectory is traveled 5 times for three different speeds, *i.e.* [1, 3, 5] mm/s, and three [0°, 30°, 60°] different yaw angle orientations (*i.e.*, relative angles between EPM and capsule).

These two cases can cover all the scenarios for a standard tele-operated endoscopic procedure depending on the distance between the EPM and the capsule. Under these
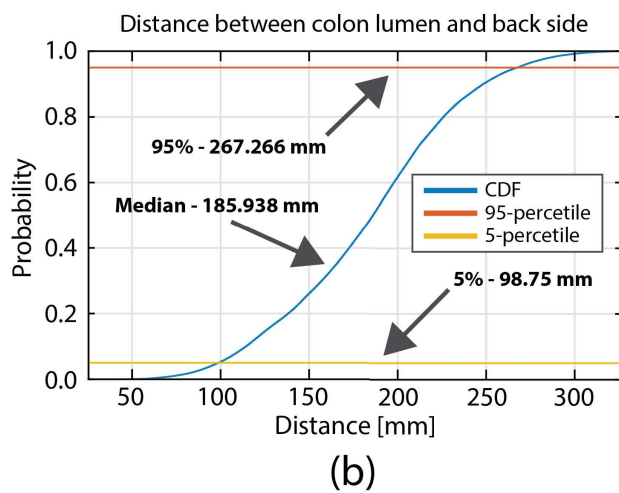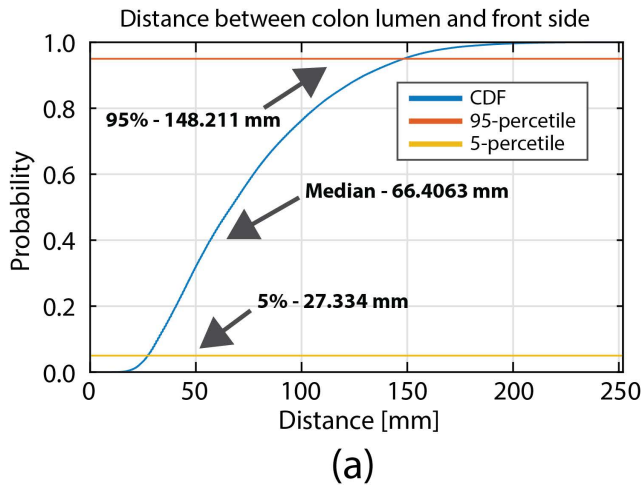
(a)

(b)

FIGURE 6. Cumulative distribution function of the distance analysis for (a) locomotion, and (b) localization purposes.

FIGURE 7. Example of a trajectory extracted from the CCT images and followed by the capsule during the searching and navigation phases. In the legend the orientations of the capsule in its reference system are indicated.

prospective, the performance evaluation has been conducted using five main components: (1) robotic platform, (2) localization module, (3) acquisition and processing sub-modules, (4) EPM with its support, and (5) endoscopic capsule with its support. The first three components remain unchanged for the two sets of tests, represented in Figure 5, while the last two vary in terms of position in the operating space, construction, and functionality of supports, as shown in Figure 5. Each module is described in detail below:

1. An accurate 6-DoF industrial robotic arm (Racer-5-0.80 robot, Comau SpA, Turin, Italy) moves the capsule/EPM along the pre-defined paths derived from the CCT-based trajectories. The robot was programmed to follow the paths at constant speeds.
2. The localization module, including the DC to AC power supply and magnetic field generation systems, was placed as closely as possible to the operating table.
3. The acquisition and elaboration sub-modules, placed under the table, are connected to the capsule to collect the 3D magnetic field and accelerometer signals, and the magnetic field generator to collect current signals.
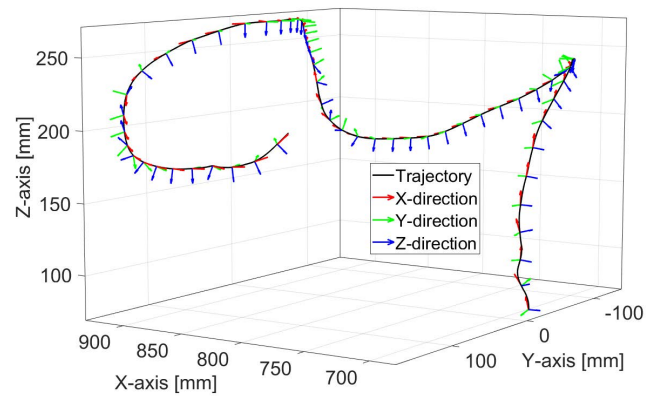
4. An EPM is placed differently based on the type of the test. During the searching phase (phase 1), it is held in a fixed pose externally to the operating work-space of the localization system. In contrast, during the navigation phase (phase 2), it is fixed on the end-effector of the robotic arm and moved to follow the predefined paths.
5. A wired endoscopic capsule fixed to a custom support, designed to change the yaw angle with a fixed step of 10°. During the searching phase, the capsule is held on the end-effector of the robotic arm, while during the navigation phase is fixed to an additional support beneath the EPM at a distance of 100 mm.

III. RESULTS

Based on the analysis of the work-space and the choices regarding the arrangement of the modules of the platform, there are a few considerations about the locomotion and localization purposes to be stated:

- *Volume*: the average dimension of the work-space, both for locomotion and localization purposes, is 220 mm, 350 mm, and 165 mm, respectively along X, Y, and Z axes according to the study mentioned in sub-section II-A about the operating distances, and using Figure 1 as reference system.
- *Locomotion*: considering a 95% confidence interval, the maximum distance between the front side and the upper surface of the colonic wall is 148.2 mm, the minimum distance is 27.3 mm, while the median distance is 66.4mm, as reported in Figure 6a.
- *Localization*: considering a 95% confidence interval, the maximum distance between the backside and the upper surface of the colonic wall is 267.3 mm, the minimum distance is 98.7 mm, while the median distance is 185.9 mm, as reported in Figure 6b.

According to the values obtained through the procedure explained in sub-section II-A for the estimation of the oper-

TABLE 1. Average deviation (mean ± confidence interval at 95%) of position for searching phase. The results are reported as the trajectory speed changes and as the algorithm progresses: outputs of the optimizations according to the spherical (SPH) and elliptical (ELL) approximations, output obtained from the mean of the previous approximations (MEAN) and final output of the algorithm (TOT).

Output Steps	Speed (mm/s)	X (mm)	Y (mm)	Z (mm)	NORM (mm)
SPH	1	6.63 ± 7.28	-8.52 ± 5.46	9.32 ± 7.61	14.46 ± 11.86
	3	7.52 ± 6.46	-7.69 ± 6.98	-8.68 ± 8.65	13.82 ± 12.86
	5	9.01 ± 5.49	8.75 ± 7.63	9.65 ± 9.09	15.84 ± 13.08
ELL	1	10.03 ± 6.85	8.65 ± 6.42	-9.28 ± 8.15	16.17 ± 12.43
	3	7.61 ± 7.03	-2.82 ± 7.60	10.68 ± 6.52	13.41 ± 12.24
	5	8.89 ± 8.28	-8.86 ± 8.75	6.79 ± 9.41	14.27 ± 15.29
MEAN	1	-4.68 ± 4.65	4.25 ± 4.65	6.42 ± 5.75	9.01 ± 8.74
	3	5.10 ± 4.82	-4.04 ± 5.72	7.36 ± 5.94	9.82 ± 9.55
	5	6.26 ± 5.47	-5.36 ± 5.01	7.46 ± 8.13	11.11 ± 11.00
TOT	1	-2.92 ± 3.53	-3.95 ± 2.66	-5.32 ± 4.58	7.24 ± 6.37
	3	3.01 ± 4.16	2.82 ± 3.09	5.68 ± 6.11	7.02 ± 8.01
	5	4.59 ± 4.41	-3.36 ± 4.09	6.79 ± 7.25	8.86 ± 9.42

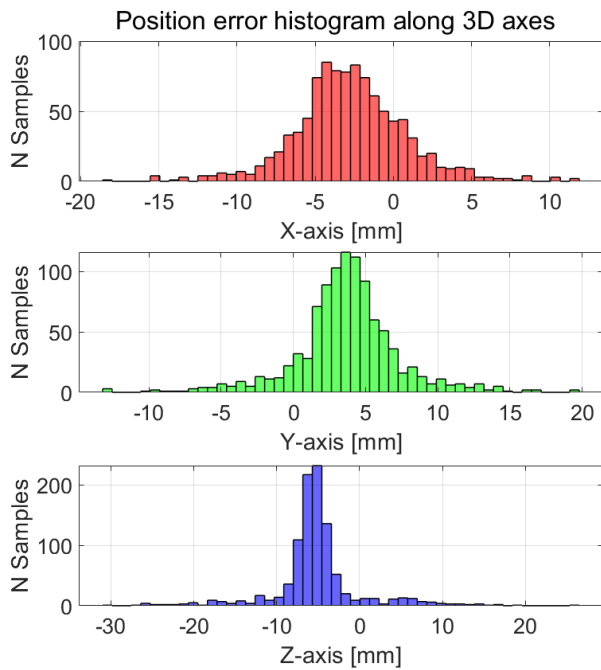**FIGURE 8.** Example of distribution of the position deviations along the 3D axes obtained during a searching phase (speed: 3 mm/s).

FIGURE 9. Example of distribution of the position and orientation error along the 3D axes obtained during a navigation phase (speed: 3 mm/s).

ational work-space, and the data obtained through the previous considerations, it was possible to design the locomotion and localization experiments by three trajectories from the CCT scans using the Matlab software, and they were selected to be followed by the endoscopic capsule during the experimental phases. Figure 7 shows an example of one of these trajectories.

Table 1 and Figure 8 show, respectively, the average position deviation and distribution along the three axes by averaging the errors obtained by executing five times the selected three trajectories during the searching phase tests. Table 1 also shows the deviations based on the progression of the position estimate in the spherical (SPH), ellipsoidal (ELL), average (MEAN), and final (TOT) optimization stages of the
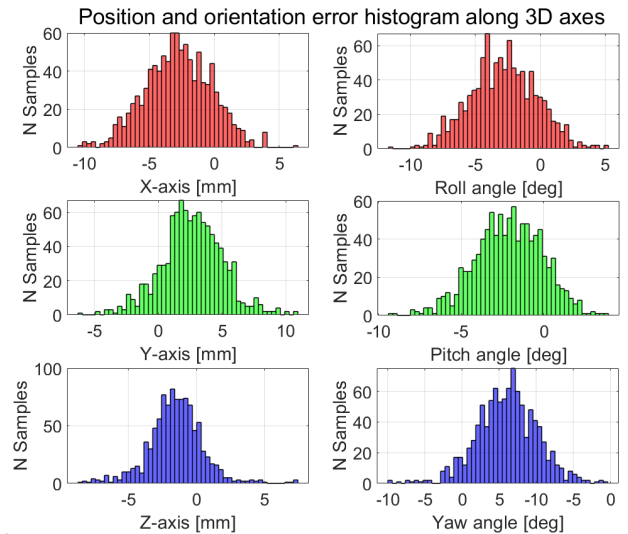
localization algorithm. The comparison between the performance of the positioning outputs was performed considering the same capsule's speed. Indeed, the average position deviation along all three axes is the lowest (p-value < 0.01) considering the final output of the algorithm (TOT). Moreover, the estimation (MEAN) obtained by averaging the outcomes of the optimizations according to the spherical (SPH) and elliptical (ELL) approximation is statistically more accurate than those calculated without the average (p-value < 0.01).

In summary, the final average position deviation (TOT) obtained in the worst case (*i.e.*, 5 mm/s speed) during the searching phase tests is 4.59 ± 4.41 mm along X-axis, −3.36 ± 4.09 mm along Y-axis, 6.79 ± 7.25 mm along Z-axis, and 8.86 ± 9.42 as the norm of all the components. As previously reported, the evaluation of the orientation error has not been carried out because, especially during the searching phase, one can assume that the capsule experiences a self-orientation because of the magnetic attraction by the

TABLE 2. Average deviation (mean ± confidence interval at 95%) of position for navigation phase. The results are reported as the trajectory speed changes and as the algorithm progresses: outputs of the optimizations according to the spherical (SPH) and elliptical (ELL) approximations, the outcome obtained from the mean of the previous approximations (MEAN), and the final output of the algorithm (TOT).

Output Steps	Speed (mm/s)	X (mm)	Y (mm)	Z (mm)	NORM (mm)
SPH	1	-7.32 ± 6.25	6.47 ± 6.88	-3.24 ± 6.34	10.28 ± 11.25
	3	-8.85 ± 6.02	3.86 ± 5.72	-4.42 ± 6.61	10.62 ± 10.61
	5	6.21 ± 5.71	7.69 ± 6.36	3.56 ± 8.43	10.51 ± 12.01
ELL	1	-8.74 ± 6.03	-7.51 ± 5.47	-5.21 ± 7.67	12.65 ± 11.19
	3	7.35 ± 6.68	3.82 ± 6.68	0.68 ± 5.63	8.31 ± 11.00
	5	-7.69 ± 6.53	-5.62 ± 6.64	4.84 ± 5.29	10.68 ± 10.72
MEAN	1	-5.88 ± 5.48	2.45 ± 3.73	2.24 ± 2.45	6.75 ± 7.07
	3	-3.65 ± 4.73	-3.40 ± 4.71	3.38 ± 3.00	6.03 ± 7.32
	5	-3.75 ± 3.80	3.34 ± 4.05	6.46 ± 3.64	8.18 ± 6.64
TOT	1	3.04 ± 2.86	3.25 ± 3.53	1.20 ± 2.89	4.61 ± 5.39
	3	2.85 ± 3.27	2.70 ± 3.59	2.34 ± 3.48	4.57 ± 5.48
	5	3.79 ± 3.81	-3.31 ± 4.09	2.49 ± 3.70	5.61 ± 6.71

TABLE 3. Average deviation (mean ± standard deviation) of orientation during the navigation phase.

Speed (mm/s)	Roll (Deg.)	Pitch (Deg.)	Yaw (Deg.)
1	2.04 ± 2.15	1.03 ± 1.93	3.20 ± 3.02
3	-1.10 ± 1.24	-0.70 ± 1.15	-3.05 ± 2.57
5	1.89 ± 2.21	-1.04 ± 2.04	1.57 ± 2.32

EPM in a large area, such as the rectum. For this reason, there was no interest in evaluating the orientation during the searching phase.

Table 2 and Figure 9 show the average position deviation and its distribution along the three axes by averaging the deviations obtained by executing five times the selected three trajectories during the navigation phase tests. Even in this case, it is possible to confirm the evaluations reported for the searching results regarding the accuracy of the output steps and output update latency. In addition, comparing the position errors shown in Table 1 and Table 2, it is possible to observe that the accuracy is higher during the navigation phase (p-value < 0.01). This improvement is caused by the presence of the EPM that represents an additional source out of the plane of the coils.

In summary, the final average position deviation (TOT) along the three axes in the worst case (*i.e.*, 5 mm/s speed) navigation phase is 3.79 ± 3.81 mm along X-axis, −3.31 ± 4.09 mm along Y-axis, 2.49 ± 3.70 mm along Z-axis, and 5.61 ± 6.71 as the norm of all the components. Once the final position estimate (TOT) was obtained, as described in the localization algorithm section, it was possible to obtain the capsule orientation estimation. Table 2 and Figure 9 show the average orientation error along the three axes by averaging the error obtained by executing five times the selected three trajectories for each yaw angle mismatch during the navigation phase. The average orientation deviation along the three axes during the worst case (*i.e.*, 5 mm/s speed)

TABLE 4. Comparison of the proposed magnetic localization strategy with respect to the state-of-the-art, compatible with high-grade magnetic field locomotion.

References	Work-Space	Update Rate (ms)	Position Accuracy	Orientation Accuracy
Salerno *et al.* [18]	200 × 200 × 120 mm^3	2700	-3.2 ± 18 mm along X 5.4 ± 15 mm along Y -13 ± 19 mm along Z	N/A
Di Natali *et al.* [19]	150 × 150 × 200 mm^3	7	6.2 ± 4.4 mm radial 6.9 ± 3.9 mm axial 5.4° ± 7.9° azimuth	0.27° ± 0.17° pitch 0.34° ± 0.18° yaw 1.8° ± 1.1° roll
Taddese *et al.* [17]	Spherical shell of ∼200 mm radius centred into EPM	10	-3.39 ± 6.76 mm along X -4.84 ± 5.23 mm along Y 4.06 ± 1.91 mm along Z	-0.96° ± 2.30° roll 0.29° ± 1.73° pitch -0.37° ± 2.84° yaw
Abbott *et al.* [27]	Spherical shell of ∼200 mm radius centred into EPM	3400	4.9 ± 2.7 mm	3.3° ± 1.7°
Xu *et al.* [28]	300 × 300 × 300 mm^3	17	5.5 ± 2.6 mm	5.2° ± 4.3°
Our proposed work	**300 × 300 × 300 mm^3** **(expandable)**	**300**	**3.79 ± 4.35 mm along X** **-3.31 ± 4.67 mm along Y** **2.49 ± 4.22 mm along Z**	**1.89° ± 2.21° roll** **-1.04° ± 2.04° pitch** **1.57° ± 2.32° yaw**

navigation phase is $1.89° \pm 2.21°$, $-1.04° \pm 2.04°$, $1.57° \pm 2.32°$ for roll, pitch and yaw angle, respectively, as shown in Table 3.

The results show that the final average pose deviations in the searching and navigation phases are compatible with a magnetic endoscopic capsule procedure, as also found in literature [15], [17]–[19]. The update rate (*i.e.*, 300 ms) does not allow a fast real-time closed-loop control, but considering the speed of a typical procedure [40], it can guarantee an efficient navigation control. The obtained results are in accordance with the state-of-the-art magnetic localization and compatible with external high-grade magnetic locomotion, as shown in Table 4. These critical aspects introduce a clear benefit in the localization accuracy as shown in Tables 2 due to the presence of an EPM in the navigation phase, compared to the results obtained in Table 1 in the absence of the EPM during the searching phase. However, even if performances are comparable (and often better) with the state-of-the-art, our system introduces benefits providing the flexibility in expanding the localization work-space by increasing the number of EMs integrated onto or below the operating table.

IV. CONCLUSION AND DISCUSSIONS

This paper proposes a hybrid 6-DoF magnetic localization system compatible with external high-grade magnetic actuation. The novel methodology and approach, which combines five magnetic field sources, exploits two triangulation steps applied in series to estimate the capsule pose accurately. Four EM sources, completely dedicated to localization, generate alternating magnetic fields at different frequencies, while the fifth is a permanent magnetic field source (EPM) used primarily for locomotion. The localization system takes advantage of the magnetic field generated by the permanent magnet source. However, the localization system is also able to find the endoscopic capsule without exploiting the EPM. As shown in Tables 1 and 2, the comparison between the searching and the navigation phases in the worst-case scenario (5 mm/s as speed) has shown no significant difference (p-value < 0.01) considering a confidence interval at 95% for the final position estimate (TOT) accuracy. The developed methodology shows consistent results with the ones found in the literature that are summarized in Table 4. This aspect guarantees that at the beginning of the procedure or when the magnetic link between EPM and capsule is absent (searching phase), it is possible to find it even without a correct positioning of the EPM that can be placed far away from the capsule (*i.e.*, initial safe position). As demonstrated by experimental tests, the presence of the EPM increases the accuracy of position estimation. Still, it does not affect the correct functionality of the localization system, although introducing a benefit in the localization accuracy of ~60% concerning the case without EPM. Furthermore, since the design phase was based on an in-depth analysis of the work-space occupied by the colon within the body, the localization system can localize the capsule in at least 95% of patients.

The use of two optimization steps reduces the laying estimation error and increases the processing speed of the algorithm. The first step provides a rough estimate of the position. It is based on two mathematical approximations of the magnetic field. On the other hand, the second step refines the estimate by minimizing the RMSD of the triangulation based on an analytical magnetic field model. Experimental tests have shown the incremental trend of accuracy in position estimation at the proceeding steps of the algorithm, both in the searching and navigation phases. In addition, tests have shown how the presence of a source that does not lie on the same plane, *i.e.* the EPM as other sources, can increase the accuracy of position estimation of ~60%. Final results in the navigation phase guarantee an average accuracy of about 5 mm and 5° in position and orientation, respectively, suitable with the capsule navigation along the colon. In fact, it must be taken into account that the dimension of a commercially-available endoscopic capsule is around 12 mm in diameter and 32 mm in length, and the colon diameter is approximately 40 mm in average [41]. Considering the localization solutions compatible with high-grade magnetic field actuation sources, the system's accuracy and update rate presented in this paper is optimal for a robotic endoscopic technology and, in several cases, even better than those found so far in the literature. In addition, our solution introduces the remarkable main benefit of expanding the localization work-space by increasing the number of EMs into the operating table.

In conclusion, the proposed innovative solution is suitable with magnetically-driven robotic endoscopic procedures and paves the way for further improvements. For instance, the usage of a neural network can enhance the performance and the accuracy of the mathematical approximations by replacing the analytical magnetic field models described in [34]. The localization accuracy could also be improved by adopting a solution that distributes the EMs in 3D configuration instead of positioning them only on a plane below the patient.

APPENDIX

In this section, a complete overview of the mathematical models of the magnetic field is provided. As previously introduced in sub-sections II-B and II-C, two different mathematical models have been employed to describe the distribution of the magnetic field intensity sensed by the magnetically-driven robotic capsule endoscope. The first source of the magnetic field is given by an EPM, which has been used to navigate the endoscope to a specific location [14]. In contrast, the second source of the magnetic field is identified as an alternating field produced by four different coils where each of them operates at different frequencies that are induced by specific currents flow, as shown in equation 2. Combining all the magnetic sources using their corresponding weights and integrating an accelerometer sensor allows estimating the capsule endoscope's position and orientation, respectively. The mathematical models regarding the EPM and the

coils are presented in sub-section IV-A and IV-B, while in sub-section IV-C a description of the mathematical approximation and the calculation of the weights is provided.

A. EPM MAGNETIC MODEL

The magnetic modeling of the EPM is based on the charge model [34]. The charge model has been used in this work to estimate and analyze the magnetic field generated by a cylindrical permanent magnet diametrical magnetized and used to guide the endoscope to a specific location. The main assumption of the charge model is to reduce a magnet to a distribution of equivalent "magnetic charge" [34]. Considering a permanent magnet in a free space, the general formulation of the corresponding generated magnetic field is given by equation 10:

$$\mathbf{B}(\mathbf{r}) = -\frac{\mu_0}{4\pi} \int_V \frac{[\nabla \cdot \mathbf{M}](\mathbf{r} - \mathbf{r}')}{|\mathbf{r} - \mathbf{r}'|^3} dV' \\ + \frac{\mu_0}{4\pi} \oint_S \frac{[\mathbf{M} \cdot \hat{\mathbf{n}}](\mathbf{r} - \mathbf{r}')}{|\mathbf{r} - \mathbf{r}'|^3} dS' \quad (10)$$

where $\mathbf{r}$ indicates the point in which the magnetic field is calculated, $\mathbf{r}'$ represents the position of the source element point that generates the magnetic field, $\mathbf{M}$ is the magnetization inherent to the source element point, $\hat{\mathbf{n}}$ is the normal vector to the surface of the source element point, dV' and dS' are the volume and surface source elements, respectively. Assuming an equivalent charge distribution that follows the equation 10, it is possible to infer that the density charge inside the volume is null. This implies that the term $\nabla \cdot \mathbf{M}$ is equal to 0. Therefore, equation 10 can be simplified, in order to calculate the magnetic field generated by a cylindrical shape with diametrical magnetization along x-axis, in the following equation 11:

$$\mathbf{B}(\mathbf{r}) = \frac{\mu_0 M_x}{4\pi} \oint \frac{\cos\theta'(\mathbf{r} - \mathbf{r}')}{|\mathbf{r} - \mathbf{r}'|^3} R d\theta' dz' \quad (11)$$

where M_x is the magnetization along the x-axis, R is the radius of the cylinder, θ' is the angle of the infinitesimal element surface location in the reference system, $d\theta'$ is the infinitesimal angle of the surface element, and dz' is the infinitesimal length of the surface element since the main axis of the cylinder is oriented along z-axis. The procedure to numerically solve the integrals in equation 11 is fully described in reference [42].

B. EMs MODEL

The magnetic model of the EMs is based on the Biot-Savart's law, introduced in equation 1, where the magnetic field is generated by an infinitesimal length element that carries a current intensity I_c. For the sake of simplicity, the main axis of the coil is the z-axis, and the current flow lays on the xy-plane. The coil is subdivided into a certain number of turns, where each of them is represented by a z_k coordinate. Each turn is divided into a radial component described as r_i, and an angular component identified as θ_j for which the current flow is parallel to the infinitesimal length element ($\mathbf{dl}$) introduced in equation 1. Based on this assumption, equation 1 can be rewritten in the following relation (equation 12):

$$\mathbf{B}(\mathbf{r}) = \frac{\mu_0 I_c}{4\pi} \sum_{i=1}^{N_i} \sum_{k=1}^{N_k} \int_0^{2\pi} \frac{\mathbf{dl_{i,j}} \times (\mathbf{r} - \mathbf{r}'_{i,j,k})}{|\mathbf{r} - \mathbf{r}'_{i,j,k}|^3} \quad (12)$$

where N_i represents the number of elements of which the radial component is divided into, and N_k indicates the number of turns in which the coil ha been subdivided. In this frame, the infinitesimal length of current element $\mathbf{dl_{i,j}}$ and the corresponding vectorial position $\mathbf{r}'_{i,j,k}$ are defined as the following equations 13-14-15:

$$\mathbf{dl_{i,j}} = -dl_i \sin\theta_j \hat{\mathbf{x}} + dl_i \cos\theta_j \hat{\mathbf{y}} \quad (13)$$

$$\mathbf{r}'_{i,j,k} = r_i \cos\theta_j \hat{\mathbf{x}} + r_i \sin\theta_j \hat{\mathbf{y}} + z_k \hat{\mathbf{z}} \quad (14)$$

$$|\mathbf{r} - \mathbf{r}'_{i,j,k}|^3 = \left[(x - r_i \cos\theta_j)^2 \\ + (y - r_i \sin\theta_j)^2 + (z - z_k)^2\right]^{\frac{3}{2}} \quad (15)$$

where dl_i is the ith element of length that carries the current flow, and it is calculated using equation 16:

$$dl_i = \frac{2\pi r_i}{N_j} \quad (16)$$

where r_i is the radial location of each element of current, and N_j represents the number of elements of which the angular component is divided into. The variables x, y, z represent the coordinates for which the magnetic field $\mathbf{B}(\mathbf{r})$ is calculated. Therefore, performing the cross product and integrating numerically equation 12, the numerical form of the relation that allows to compute the magnetic field generated by a coil to a specific point ($\mathbf{r}$) is given by equation 17:

$$\mathbf{B}(\mathbf{r}) = \frac{\mu_0 I_c}{4\pi} \sum_{i=1}^{N_i} \sum_{k=1}^{N_k} \sum_{j=1}^{N_j} \left\{ \left[\frac{dl_i \cos\theta_j \cdot (z - z_k)}{|\mathbf{r} - \mathbf{r}'_{i,j,k}|^3} \right] \hat{\mathbf{x}} \\ + \left[\frac{dl_i \sin\theta_j \cdot (z - z_k)}{|\mathbf{r} - \mathbf{r}'_{i,j,k}|^3} \right] \hat{\mathbf{y}} \\ - \left[\frac{dl_i \cos\theta_j \cdot (x - r_i \cos\theta_j)}{|\mathbf{r} - \mathbf{r}'_{i,j,k}|^3} \right. \\ \left. + \frac{dl_i \sin\theta_j \cdot (y - r_i \sin\theta_j)}{|\mathbf{r} - \mathbf{r}'_{i,j,k}|^3} \right] \hat{\mathbf{z}} \right\} \quad (17)$$

C. MATHEMATICAL APPROXIMATION AND WEIGHTS

In this section, a description of the mathematical approximations of the analytical magnetic models (sub-sections A and B of the Appendix) is provided. The purpose of implementing these mathematical approximations is to increase the performance of the localization algorithm described in sub-section II-C. The mathematical approximation consists

of developing logistic functions that emulate the behavior of the three components of the magnetic field scalar intensity and estimate the corresponding distances between the source and the target point where the magnetic field is computed. The general formulation of the logistic functions is shown in equation 18:

$$d_i = \alpha_i |\mathbf{B(r)}|^{\beta_i} + \gamma_i \qquad (18)$$

where d_i is the calculated distance in dependence of the calculated magnetic field scalar intensity $|\mathbf{B(r)}|$, and the terms α_i, β_i, and γ_i represent the parameters that are obtained from the analytical models described in sub-sections A and B of the Appendix. These parameters are fitted using the analytical models to compute the parameters by comparing the model with the measured data. The index i indicates the three axial components x, y, and z. The distance values d_i are used as fixed parameters in the spherical (SPH) and ellipsoidal (ELL) optimizations introduced in sub-section II-C. Particularly for the ellipsoidal approximation (see equation 4), the variable $d_\perp$ and $d_\parallel$ are computed through equation 19:

$$d_\perp = \sqrt{d_x^2 + d_y^2}, \quad d_\parallel = d_z. \qquad (19)$$

The logistic functions defined in equation 18, are also employed to define weights (w_n) that are used in the objective functions to solve the minimization problems (see equation 3-4-8). The weights are calculated using equation 20:

$$w_n = \left[min_i \left(\frac{1}{d_i^+ - d_i^-} \right) \right]_n \qquad (20)$$

where the subscript n indicates the magnetic source and the index i represents the three axial components. The variables d_i^+, and d_i^- are calculated using equation 18 with the following modification (equation 21):

$$d_i^\pm = \alpha_i \left(|\mathbf{B(r)}| \pm dB \right)^{\beta_i} + \gamma_i \qquad (21)$$

where dB is a small step value of magnetic field, typically 0.1% of the value $|\mathbf{B(r)}|$ used to calculate the high d_i^+ and low d_i^- distances needed in equation 20. Finally, the three axial components' minimum value has been chosen to represent the weights w_n for each magnetic source.

ACKNOWLEDGMENT

REFERENCES

[1] H. Sung, J. Ferlay, R. L. Siegel, M. Laversanne, I. Soerjomataram, A. Jemal, and F. Bray, "Global cancer statistics 2020: GLOBOCAN estimates of incidence and mortality worldwide for 36 cancers in 185 countries," *CA A, Cancer J. Clinicians*, vol. 71, no. 3, pp. 209–249, May 2021.

[2] *Cancer Statistics Review, 1975-2018—SEER Statistics*. Accessed: Dec. 20, 2021. [Online]. Available: https://seer.cancer.gov/csr/1975_2018/

[3] C. Hassan, P. G. Rossi, L. Camilloni, D. K. Rex, B. Jimenez-Cendales, E. Ferroni, P. Borgia, A. Zullo, G. Guasticchi, and H. Group, "Meta-analysis: Adherence to colorectal cancer screening and the detection rate for advanced neoplasia, according to the type of screening test," *Alimentary Pharmacol. Therapeutics*, vol. 36, no. 10, pp. 929–940, Nov. 2012.

[4] G. Iddan, G. Meron, A. Glukhovsky, and P. Swain, "Wireless capsule endoscopy," *Nature*, vol. 405, p. 417, May 2000.

[5] C. A. Tennyson and B. S. Lewis, "Capsule endoscopy," in *Textbook of Clinical Gastroenterology and Hepatology* . Hoboken, NJ, USA: Wiley, 2012.

[6] L. J. Sliker and G. Ciuti, "Flexible and capsule endoscopy for screening, diagnosis and treatment," *Expert Rev. Med. Devices*, vol. 11, no. 6, pp. 649–666, Nov. 2014.

[7] G. Ciuti, R. Caliò, D. Camboni, L. Neri, F. Bianchi, A. Arezzo, A. Koulaouzidis, S. Schostek, D. Stoyanov, C. M. Oddo, and B. Magnani, "Frontiers of robotic endoscopic capsules: A review," *J. Micro-Bio Robot.*, vol. 11, no. 1, pp. 1–18, 2016.

[8] G. Cummins, B. F. Cox, G. Ciuti, T. Anbarasan, M. P. Y. Desmulliez, S. Cochran, R. Steele, J. N. Plevris, and A. Koulaouzidis, "Gastrointestinal diagnosis using non-white light imaging capsule endoscopy," *Nature Rev. Gastroenterol. Hepatol.*, vol. 16, no. 7, pp. 429–447, Jul. 2019.

[9] M. Voska, M. Zavoral, T. Grega, O. Majek, J. Martinek, I. Tacheci, M. Benes, G. Vojtechova, P. Drastich, J. Bures, J. Spicak, B. Buckova, O. Ngo, and S. Suchanek, "Accuracy of colon capsule endoscopy for colorectal neoplasia detection in individuals referred for a screening colonoscopy," *Gastroenterol. Res. Pract.*, vol. 2019, pp. 1–8, Sep. 2019.

[10] C. Spada, S. F. Pasha, S. A. Gross, J. A. Leighton, F. Schnoll-Sussman, L. Correale, B. G. Suárez, G. Costamagna, and C. Hassan, "Accuracy of first- and second-generation colon capsules in endoscopic detection of colorectal polyps: A systematic review and meta-analysis," *Clin. Gastroenterol. Hepatol.*, vol. 14, no. 11, pp. 1533–1543, 2016.

[11] G. Ciuti, K. Skonieczna-Żydecka, W. Marlicz, V. Iacovacci, H. Liu, D. Stoyanov, A. Arezzo, M. Chiurazzi, E. Toth, H. Thorlacius, P. Dario, and A. Koulaouzidis, "Frontiers of robotic colonoscopy: A comprehensive review of robotic colonoscopes and technologies," *J. Clin. Med.*, vol. 9, no. 6, p. 1648, May 2020.

[12] W. Marlicz, X. Ren, A. Robertson, K. Skonieczna-Żydecka, I. Łoniewski, P. Dario, S. Wang, J. N. Plevris, A. Koulaouzidis, and G. Ciuti, "Frontiers of robotic gastroscopy: A comprehensive review of robotic gastroscopes and technologies," *Cancers*, vol. 12, no. 10, p. 2775, Sep. 2020.

[13] F. Bianchi, A. Masaracchia, E. S. Barjuei, A. Menciassi, A. Arezzo, A. Koulaouzidis, D. Stoyanov, P. Dario, and G. Ciuti, "Localization strategies for robotic endoscopic capsules: A review," *Expert Rev. Med. Devices*, vol. 16, no. 5, pp. 381–403, May 2019.

[14] G. Ciuti, P. Valdastri, A. Menciassi, and P. Dario, "Robotic magnetic steering and locomotion of capsule endoscope for diagnostic and surgical endoluminal procedures," *Robotica*, vol. 28, no. 2, pp. 199–207, Mar. 2010.

[15] A. W. Mahoney and J. J. Abbott, "Generating rotating magnetic fields with a single permanent magnet for propulsion of untethered magnetic devices in a lumen," *IEEE Trans. Robot.*, vol. 30, no. 2, pp. 411–420, Apr. 2014.

[16] G. Lucarini, M. Mura, G. Ciuti, R. Rizzo, and A. Menciassi, "Electromagnetic control system for capsule navigation: Novel concept for magnetic capsule maneuvering and preliminary study," *J. Med. Biol. Eng.*, vol. 35, no. 4, pp. 428–436, 2015.

[17] A. Z. Taddese, P. R. Slawinski, M. Pirotta, E. De Momi, K. L. Obstein, and P. Valdastri, "Enhanced real-time pose estimation for closed-loop robotic manipulation of magnetically actuated capsule endoscopes," *Int. J. Robot. Res.*, vol. 37, no. 8, pp. 890–911, Jul. 2018.

[18] M. Salerno, G. Ciuti, G. Lucarini, R. Rizzo, P. Valdastri, A. Menciassi, A. Landi, and P. Dario, "A discrete-time localization method for capsule endoscopy based on on-board magnetic sensing," *Meas. Sci. Technol.*, vol. 23, no. 1, 2012, Art. no. 015701.

[19] C. Di Natali, M. Beccani, N. Simaan, and P. Valdastri, "Jacobian-based iterative method for magnetic localization in robotic capsule endoscopy," *IEEE Trans. Robot.*, vol. 32, no. 2, pp. 327–338, Apr. 2016.

[20] C. Hu, M. Q.-H. Meng, and M. Mandal, "Efficient magnetic localization and orientation technique for capsule endoscopy," *Int. J. Inf. Acquisition*, vol. 2, no. 1, pp. 23–36, Mar. 2005.

[21] C. Hu, Y. Ren, X. You, W. Yang, S. Song, S. Xiang, X. He, Z. Zhang, and M. Q.-H. Meng, "Locating intra-body capsule object by three-magnet sensing system," *IEEE Sensors J.*, vol. 16, no. 13, pp. 5167–5176, Jul. 2016.

[22] M. Wang, Q. Shi, S. Song, and M. Q.-H. Meng, "A novel magnetic tracking approach for intrabody objects," *IEEE Sensors J.*, vol. 20, no. 9, pp. 4976–4984, May 2020.

[23] A. Plotkin and E. Paperno, "3-D magnetic tracking of a single subminiature coil with a large 2-D array of uniaxial transmitters," *IEEE Trans. Magn.*, vol. 39, no. 5, pp. 3295–3297, Sep. 2003.

[24] T. Nagaoka and A. Uchiyama, "Development of a small wireless position sensor for medical capsule devices," in *Proc. 26th Annu. Int. Conf. Eng. Med. Biol. Soc.*, vol. 1, Sep. 2004, pp. 2137–2140.

[25] M. N. Islam and A. J. Fleming, "A novel and compatible sensing coil for a capsule in wireless capsule endoscopy for real time localization," in *Proc. IEEE SENSORS*, Nov. 2014, pp. 1607–1610.

[26] A. Sorriento, M. B. Porfido, S. Mazzoleni, G. Calvosa, M. Tenucci, G. Ciuti, and P. Dario, "Optical and electromagnetic tracking systems for biomedical applications: A critical review on potentialities and limitations," *IEEE Rev. Biomed. Eng.*, vol. 13, pp. 212–232, 2020.

[27] K. M. Popek, T. Hermans, and J. J. Abbott, "First demonstration of simultaneous localization and propulsion of a magnetic capsule in a lumen using a single rotating magnet," in *Proc. IEEE Int. Conf. Robot. Autom. (ICRA)*, May 2017, pp. 1154–1160.

[28] Y. Xu, Z. Zhao, K. Li, and M. Q.-H. Meng, "Towards external sensor based simultaneous magnetic actuation and localization for WCE," in *Proc. IEEE Int. Conf. Robot. Biomimetics (ROBIO)*, Dec. 2019, pp. 2332–2337.

[29] M. Verra, A. Firrincieli, M. Chiurazzi, A. Mariani, G. L. Secco, E. Forcignanò, A. Koulaouzidis, A. Menciassi, P. Dario, G. Ciuti, and A. Arezzo, "Robotic-assisted colonoscopy platform with a magnetically-actuated soft-tethered capsule," *Cancers*, vol. 12, no. 9, p. 2485, Sep. 2020.

[30] (2019). *Endoo EU Project*. [Online]. Available: https://cordis.europa.eu/project/id/688592

[31] G. Ciuti, P. Dario, F. Bianchi, A. Masaracchia, E. S. Barjuei, and J. O. Alcaide, "System for the magnetic localization and locomotion of an endoscopic capsule," WO 2021 005 582 (A1), Aug. 11, 2019. [Online]. Available: https://worldwide.espacenet.com/publicationDetails/biblio?DB=EPODOC&II=0&ND=3&adjacent=true&locale=en_EP&FT=D&date=20210114&CC=WO&NR=20210055 82A1&KC=A1

[32] J. Li, E. S. Barjuei, G. Ciuti, Y. Hao, P. Zhang, A. Menciassi, Q. Huang, and P. Dario, "Magnetically-driven medical robots: An analytical magnetic model for endoscopic capsules design," *J. Magn. Magn. Mater.*, vol. 452, pp. 278–287, Apr. 2018.

[33] Data From CT Colonography. (2015). *The Cancer Imaging Archive*. [Online]. Available: https://wiki.cancerimagingarchive.net/display/Public/CT+COLONOGRAPHY

[34] E. Furlani, *Permanent Magnet and Electromechanical Devices: Materials, Analysis, and Applications* (Electromagnetism). Amsterdam, The Netherlands: Elsevier, 2001.

[35] J. Cooley, P. Lewis, and P. Welch, "The finite Fourier transform," *IEEE Trans. Audio Electroacoustics*, vol. AE-17, no. 2, pp. 77–85, Jun. 1969.

[36] C. G. Broyden, "The convergence of a class of double-rank minimization algorithms 1. General considerations," *IMA J. Appl. Math.*, vol. 6, no. 1, pp. 76–90, 1970.

[37] T. C. Lee, R. L. Kashyap, and C. N. Chu, "Building skeleton models via 3-D medial surface axis thinning algorithms," *CVGIP, Graph. Models Image Process.*, vol. 56, no. 6, pp. 462–478, 1994.

[38] P. Kollmannsberger, M. Kerschnitzki, F. Repp, W. Wagermaier, R. Weinkamer, and P. Fratzl, "The small world of osteocytes: Connectomics of the lacuno-canalicular network in bone," *New J. Phys.*, vol. 19, no. 7, Jul. 2017, Art. no. 073019.

[39] (2017). *Skeleton3d*. [Online]. Available: https://github.com/phi-max/skeleton3d-MATLAB

[40] L. J. Sliker, G. Ciuti, M. E. Rentschler, and A. Menciassi, "Frictional resistance model for tissue-capsule endoscope sliding contact in the gastrointestinal tract," *Tribol. Int.*, vol. 102, pp. 472–484, Oct. 2016.

[41] A. Alazmani, A. Hood, D. Jayne, A. Neville, and P. Culmer, "Quantitative assessment of colorectal morphology: Implications for robotic colonoscopy," *Med. Eng. Phys.*, vol. 38, no. 2, pp. 148–154, Feb. 2016.

[42] E. Furlani, *Permanent Magnet Electromechanical Devices: Mater., Anal., Appl.* (Electromagnetism). Amsterdam, The Netherlands: Elsevier Science, 2001.

FEDERICO BIANCHI received the B.Sc. and M.Sc. degrees in biomedical engineering from the University of Pisa, Pisa, Italy, and the Ph.D. degree in biorobotics from Scuola Superiore Sant'Anna, Pisa. He is currently with the Competence Centre in Industry 4.0 (ARTES 4.0—Advanced Robotics and Enabling Digital Technologies and Systems), as the responsible of the robotics platforms. He was a Collaborator in the EU Endoo Project (H2020-ICT-24-2015) and in other research activities with the Beijing Advanced Innovation Center for Intelligent Robots and Systems, about the development of an innovative endoscopic robotic platform for painless colonoscopy. His research interests included collaborative medical robotic platforms, such as tele-operated magnetic-based robotic platforms and localization and navigation of intraluminal robots.

ANTONINO MASARACCHIA (Member, IEEE) received the Ph.D. degree in electronics and telecommunications engineering from the University of Palermo, Italy, in 2016. His Ph.D. studies were conducted in joint supervision with the Institute of Informatics and Telematics (IIT), National Research Council (CNR), Pisa, Italy, and the obtained results have been important contributions from IIT to the FP7-MOTO European Project. From 2017 to 2018, he was a Postdoctoral Researcher at the Sant'Anna School of Advanced Studies, The BioRobotics Institute, where in the context of the European Project Endoo, he conducted research activities for the development of a localization module based on the usage of alternating magnetic fields. Since September 2018, he has been a Research Fellow with the Centre for Wireless Innovation, Queens University Belfast, U.K. His research interests include fifth generation (5G) and beyond 5G networks, convex optimization and applied machine learning techniques to wireless communications, reconfigurable intelligent surfaces (RIS), UAV-enabled networks, and ultra-reliable and low-latency communications (URLLC). He was awarded with the Seal of Excellence delivered from the European Commission for his project submitted to Marie Skłodowska-Curie Actions Call H2020-MSCA-IF-2020. He is currently serving as a Guest Editor for *EAI Endorsed Transactions on Industrial Networks and Intelligent Systems* and a Special Issue on Radio Frequency Energy Harvesting and Wireless Power Transfer published by *Electronics* (MDPI) for which he serves also as a Topic Editor. He serves as a Guest Editor for a Special Issue on Controls, Communications and Networking for Ad-Hoc Mobile Sensor Networks published by *ICSES Transactions on Computer Networks and Communications*. He has served as a Guest Editor for a Special Issue on Reliable Communication for Emerging Wireless Networks published by *Mobile Networks and Applications* (ACM/Springer).

ANGELO DAMONE received the M.Sc. degree in chemistry from the University of Bari, Bari, Italy, in 2013, with a thesis titled "Molecular Dynamics of Metals with Applications in the Field of Nuclear Fusion," and the Ph.D. degree in molecular dynamics, in 2017, defending a thesis titled "Hybrid Atomistic-Continuum Modeling of Liquid-Liquid Interface by Molecular Dynamics." He developed a molecular dynamics code from scratch to model the negative hydrogen ions production in the neutral beam injector (NBI), collaborating with Consorzio RFX in Padova, Padova, Italy. During his Ph.D. degree at the University of Brescia, Brescia, Italy, he studied transport properties' behavior in liquid-liquid interfaces by analyzing their intrinsic shear viscosity, thermal conductivity, and self-diffusion coefficient. The project was carried out in collaboration with the Massachusetts Institute of Technology (MIT), USA, to analyze the physics of immiscible fluid displacement in a nano-scale scenario. He employed equilibrium and non-equilibrium molecular simulations to estimate transport properties using the Green-Kubo formalism. In 2018, he joined as a Postdoctoral Researcher at the Technical University of Kaiserslautern, Germany, to model force fields on a transferable scale for the so-called poly(oxymethylene)-dimethyl-ethers (OMEs). The project involved the usage of *ab-initio* calculations in determining the equilibrium geometry and the partial electric charges for the OMEs. Finally, optimization software allowed him to define the force field parameters, such as ε (minimum energy) and σ (atomic distance). In 2019, he worked as a Postdoctoral Researcher at the French Institute of Petroleum (IFPEN), Paris, France, carrying out a project about developing a computer model of electrolytes using dissipative particle dynamics (DPD). The project involved studying transport properties and optimizing DPD parameters to create a database, where competent people can predict aqueous electrolyte solutions behavior. In 2020, he joined as a Postdoctoral Researcher at Scuola Superiore Sant'Anna, Pisa, Italy, focused on several projects involving the magnetic design of endoscopic capsules, development of algorithms for endoscopic capsule localization, and numerical modeling.

ERFAN SHOJAEI BARJUEI received the B.Sc. degree in electrical engineering from Azad University, Iran, in 2006, the M.Sc. degree in mechatronics engineering from the Sharif University of Technology, Iran, in 2008, and the Ph.D. degree in industrial and information engineering from the University of Udine, Italy, in 2016. In 2015, he was a Research Intern at Karlstad University, Sweden. He has been participating in the Endoo Project at The BioRobotics Institute, Scuola Superiore Sant'Anna, Pisa, Italy, as a Research Associate, since January 2016. The main focus of his activities was on the development of analytical models for permanent and alternating magnetic fields and the design of a magnetic localization strategy for endoscopic capsules. Later on, he joined the Department of Advanced Robotics, Italian Institute of Technology (IIT), Genova, Italy. His research interests include modeling and control of mechatronic systems.

CALOGERO MARIA ODDO (Senior Member, IEEE) was born in 1983. He received the B.Sc. and M.Sc. degrees in electronic engineering from the University of Pisa (UNIPI), the Ph.D. degree in biorobotics from Scuola Superiore Sant'Anna (SSSA), the first and second level degrees (Hons.) in industrial and information engineering from SSSA (ten positions and 334 applicants). He is currently an Associate Professor of bioengineering and coordinates the Neuro-Robotic Touch Laboratory (20 research fellows), The BioRobotics Institute, SSSA. He holds courses on natural and artificial senses and neuromorphic engineering for B.Sc., M.Sc., and Ph.D. students at SSSA and UNIPI. He has over 65 conference and journal publications and a growing track record in integrating biorobotics and neuroscience, with particular interests in the study of the human sense of touch and on its artificial engineering, and in this field, he has authored high-impact publications. He has a growing portfolio of successful research grants and he was/is a Co-PI or a WP Leader within EU-H2020, EU-FP7, and national projects. He has H-index of 27 and a total of more than 4000 citations (source: Scholar). In 2016, he served as a Senior Advisor of the FET-Flagships Interim Evaluation Panel appointed by the European Commission. He was a recipient of the Working Capital grant with the SensAlone Project, funded by Telecom Italia Company (30 grants and 2133 applicants). In 2012, he was a Finalist in the "Georges Giralt Ph.D. Award," the most important European Ph.D. award in robotics, organized by EURON, the "EUropean RObotics research Network," and in 2009, he was a Finalist for the Best Student Paper Award at the IEEE Conference on Robotics and Biomimetics.

PAOLO DARIO (Life Fellow, IEEE) received the Dr.Eng. degree in mechanical engineering from the University of Pisa. He is currently a Professor of biomedical robotics and a Coordinator of the Ph.D. Program in biorobotics at Scuola Superiore Sant'Anna, Pisa, Italy. He has been and is a Visiting Researcher, a Professor, and a fellow at various universities and scientific institutions in Europe, USA, the Middle East, and Asia. His current research interests include bio-robotics and bionics, surgical robotics, micro/nano devices for endoscopy, bio-inspired devices and systems, and assistive and companion robots. He is the author of more than 400 journal publications (Scopus) and his H-Index is 59 (Scopus). In March 2015, he was identified by the *IEEE Robotics and Automation Magazine* as the Second Most Influential Scientist in robotics worldwide according to degree centrality and bibliometric criteria. He is the coauthor of more than 50 international patents and a co-founder of five start-up companies. He has been the coordinator of many large national and European projects. He served as the editor-in-chief, an associate editor, and a member for the editorial board of many international journals in biomedical engineering and in robotics. He is a fellow of the European Society on Medical and Biological Engineering. He served as the President for the IEEE Robotics and Automation Society. He received many prizes and awards, including the 1996 Joseph Engelberger Award for Medical Robotics, the 2014 IEEE RAS George Saridis Leadership Award, and the 2017 IEEE RAS Pioneer Award for Biorobotics. He is the Founding Editorial Board Member of the journal *Science Robotics* and an Associate Editor of the IEEE Transactions on Biomedical Engineering. In 2018, he has been nominated as the Editor-in-Chief of the new IEEE Transactions on Medical Robotics and Bionics.

GASTONE CIUTI (Senior Member, IEEE) received the master's degree (Hons.) in biomedical engineering from the University of Pisa, Pisa, Italy, in 2008, and the Ph.D. degree in biorobotics (Hons.) from The BioRobotics Institute, Scuola Superiore Sant'Anna, Pisa, in 2011. He is currently an Associate Professor at The BioRobotics Institute, leading the Healthcare Mechatronics Laboratory. He was actively involved in different national and international research projects, such the EU H2020 Endoo Project (www.endoo-project.eu). He is the co-author of more than 95 international peer reviewed papers on computer-integrated platforms for medical and collaborative robotics. He is also inventor of more than 10 patents. He has H-index of 27 and a total of more than 2850 citations (source: Scholar). His research interests include robot/computer-assisted platforms, such as tele-operated magnetic-based robotic platforms for navigation, localization and tracking of smart and innovative devices for guided, and focused and targeted minimally invasive surgery and diagnosis, such as in advanced capsule endoscopy and cardiovascular surgery.

● ● ●